

Article

Submarine Morphological Description of the Ancient Archipelagic Aprons in the Marcus–Wake Seamount Group, Northwestern Pacific Ocean

Xiao Wang ¹, Huaiming Li ^{1,2,*}, Yongshou Cheng ³, Pengfei Yao ¹, Fengyou Chu ¹, Weilin Ma ¹, Hongyi Wang ², Shihui Lv ⁴, Xiaohu Li ¹, Zhenggang Li ¹, Weiyan Zhang ¹ and Yanhui Dong ¹

¹ Key Laboratory of Submarine Geosciences, Second Institute of Oceanography, Ministry of Natural Resources, Hangzhou 310012, China; wangxiao@sio.org.cn (X.W.); yaopf@sio.org.cn (P.Y.); chu@sio.org.cn (F.C.); weilin_ma@sio.org.cn (W.M.); xhli@sio.org.cn (X.L.); lizg@sio.org.cn (Z.L.); zwy885@163.com (W.Z.); dongyh@sio.org.cn (Y.D.)

² Beijing Pioneer High-Tech Corporation, Beijing 100081, China; sallywang166@sina.com

³ National Marine Data Information Center, Tianjin 300012, China; yshcheng@163.com

⁴ School of Ocean Sciences, China University of Geosciences (Beijing), Beijing 100083, China; lvshihui@cugb.edu.cn

* Correspondence: huaiming_lee@163.com

Abstract: Herein, the morphological characteristics of submarine archipelagic aprons were presented for five guyots, Suda, Arnold, Lamont, Niulang, and Zhinyv, which are over 80 Ma years old and are located in the Marcus–Wake seamount group, northwestern Pacific Ocean. Nearly 28 landslide deposits were recognized using the bathymetry and backscatter intensity data collected from the studied guyots. Landslides and their deposits that surround seamounts are mostly related to the morphology of debris avalanches, scarps, gullies/channels, and bedforms. The morphology of the archipelagic aprons of the studied guyots indicates mutual landslide processes, including slump and distinct debris avalanches arising from a cohesive or cohesionless landslide material flow. The superimposition of debris flows and sedimentation dominates the recent stages of the studied guyots. The archipelagic aprons corresponding to convex-arc-shaped scarps exhibit larger domains compared to the invagination-arc-shaped scarps with similar lateral lengths. The scarp morphologies of the studied guyots are predominantly of the complex-arc shape, indicating multiple landslide events. Parallel and convergent gullies and channels are mostly found on the elongated landslide deposits, whereas divergent and radial gullies and channels are mostly distributed on the fan-shaped aprons. Ubiquitous sediment waves occurred on the bedforms of the distal archipelagic apron across the studied guyots because of sediment creep. Small-scale sediment waves were only observed in the channels on the aprons of the Suda guyot.

Keywords: archipelagic apron; morphology; landslide; Marcus–Wake seamount group; northwestern Pacific Ocean



Citation: Wang, X.; Li, H.; Cheng, Y.; Yao, P.; Chu, F.; Ma, W.; Wang, H.; Lv, S.; Li, X.; Li, Z.; et al. Submarine Morphological Description of the Ancient Archipelagic Aprons in the Marcus–Wake Seamount Group, Northwestern Pacific Ocean. *J. Mar. Sci. Eng.* **2024**, *12*, 670. <https://doi.org/10.3390/jmse12040670>

Academic Editor: Dimitris Sakellariou

Received: 12 March 2024

Revised: 5 April 2024

Accepted: 9 April 2024

Published: 18 April 2024



Copyright: © 2024 by the authors. Licensee MDPI, Basel, Switzerland. This article is an open access article distributed under the terms and conditions of the Creative Commons Attribution (CC BY) license (<https://creativecommons.org/licenses/by/4.0/>).

1. Introduction

The northwestern (NW) Pacific Ocean is characterized by the presence of numerous seamounts, such as guyots, knolls, and islands [1], which are hosted by the oldest oceanic crust on Earth [2]. Seamounts in the NW Pacific Ocean exhibit unique geological structures and morphologies due to strong and long-period geological processes, resulting in specific physical and chemical oceanographic environments in their vicinity [3,4]. Previous investigations indicated that deep-sea seamounts contained substantial critical metal mineral resources, such as ferromanganese nodules and crusts, and resources for fisheries in the NW Pacific Ocean [4–7]. Moreover, seamounts represent a prominent area of research interest in the fields of deep-sea biodiversity, ecosystems, and microbial resources [8,9].

The formation and evolution of seamounts are influenced by endogenous and exogenous processes: endogenous processes include the eruption and intrusion of magma from mantle hotspots [10], while exogenous processes include seamount landslides, weathering, and erosion caused by ocean currents [11]. The morphological characteristics of seamounts can provide crucial evidence for the study of dynamic processes associated with seamount formation [10,12]. The slope failure of seamounts can occur at any stage of submarine volcanoes because of external pressure and internal strength changes, and it can transport materials downslope for hundreds or even thousands of kilometers [13,14]. The superimposition of landslides and sedimentation leads to the unique geomorphology around seamounts and islands [3,15,16]. Landslides refer to the movement of seamount blocks caused by slope failure and can be categorized into debris avalanches, debris flows, slumps, and rock failures [3,17]. The materials generated by landslides are an important source for the formation of archipelagic aprons surrounding seamounts [14,18]. Slumps may involve multiple slope failures occurring over an extended period and represent the overall downward movement of a block along the failure surface, and during the process of moving, the block constantly breaks. Debris avalanches comprise rock debris or blocks that are transported from the source to deposits, and their striking difference with slumps is the lack of a clear slide surface. Rock failure refers to the collapse of a mountain under the influence of gravity [14,17].

Channels and gullies primarily develop on the slopes of seamounts and are formed through erosion by gravity flow [17,19]. In contrast, aprons primarily form on the lower slopes of seamounts and serve as the primary accumulation areas for landslides and sediments [20]. Debris and blocks are transported from scarps to the aprons [14], contributing to the formation of relatively flat terrain and hard-bottom areas [7,21]. In addition, bedforms that comprise sediment wave deposits primarily develop at the end of aprons or within gullies and channels [3,22]. There are ~43,000 seamounts in the global deep sea, with heights exceeding 1000 m [23]. However, only a limited number of younger seamounts, such as the Madeira archipelago, which is 10 Ma years old [17]; the Selvagens archipelago, which is 3.4 Ma years old [24]; the Nekton Ridge and French Frigate Shoals, which are 10 Ma years old [3]; and the Comoros archipelago, which is 10 Ma years old [12], have been extensively studied. There were very few studies found on archipelagic aprons resulting from the long-history evolution of ancient seamounts over 80 Ma years old. Here, we utilized the multibeam bathymetry and backscatter intensity data collected by Chinese Dayang Cruises on the five guyots of the Marcus–Wake seamount group, namely, Suda, Arnold, Lamont, Niulang, and Zhinyv, to study the geomorphology of scarps, gullies, channels, and bedforms and their influence on the archipelagic aprons. This study aims to provide valuable insights for deep-sea seamount mineral resource assessment as well as biodiversity and genetic resource investigation in seamounts of the NW Pacific Ocean.

2. Geological Background

The geomorphology of the NW Pacific Ocean seafloor is remarkable because of the presence of a considerable number of seamounts, particularly large guyots and ridges, debris aprons at the bases of volcanic edifices, and abyssal intermontane basins [25]. The volcanic edifices formed by hotspot mantle plumes during the Late Jurassic through the Late Cretaceous period and along seafloor spreading centers for about the past 190 Ma years [4,26,27] changed the structure of the original oceanic crust [28], which resulted in western-striking features including seamount chains, ridge alignments, and so on. And basalt samples collected from the seamounts of the NW Pacific Ocean exhibit isotope characteristics similar to those in the South Pacific [29,30]. Both reflect the northwesterly movement of the Pacific plate over the past 43 million years [31].

The regions around seamounts in the NW Pacific Ocean are mostly covered by calcareous sediments, primarily from the Middle and Late Cretaceous period, followed by siliceous sediment from the Paleogene period [29,30]. The surface of the deep-sea basin is primarily covered by clay [32]. The fracture zones of the NW Pacific Ocean predominantly

exhibit northwest–southeast and northeast–southwest orientations [33]. The studied guyots, namely, the Suda, Arnold, Lamont, Niulang, and Zhinyv guyots, are primarily situated in the central region of the Marcus–Wake seamount group (Figure 1). These guyots exhibit common characteristics, such as having flat tops with summit depths of ~1500 m, and their ages range from 80 to 100 Ma. The presence of archipelagic aprons, formed as a result of slope failures and landslides, is widespread around these guyots [18].

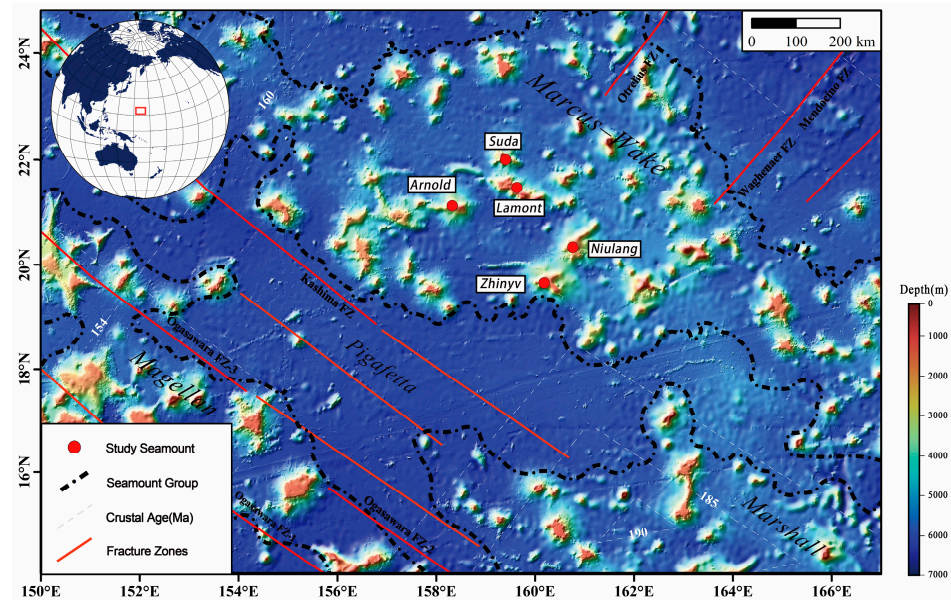


Figure 1. Bathymetric map of the Marcus–Wake seamount group, NW Pacific Ocean. Red circles mark the studied seamounts. Bathymetry data are from the General Bathymetric Chart of the Ocean [34]. Oceanic crust ages are from Müller et al. [26], and fracture zones are from Nakanishi et al. [33]. The upper-left inset shows the location of the study area.

3. Data and Methods

Multibeam survey data, including bathymetry and backscatter intensity (BI) with a resolution of ~60 m, were utilized in this study. They were obtained from several Chinese Dayang Cruises launched by the China Ocean Mineral Resources Research & Development Association from 2012 to 2022 (Table 1). Global bathymetric data with a resolution of ~15'' obtained from the General Bathymetric Chart of the Oceans (GEBCO) [34] were also incorporated.

Table 1. Sources of multibeam survey.

Study Areas	Acquisition Time	Data Sources	Type(s) of Sonar
Suda guyot	2018	Chinese DY48 Cruise	EM122
Arnold and Lamont guyots	2009	Chinese DY27 Cruise	EM122
Niulang and Zhinyv guyots	2004	Chinese DY105-12/14 Cruise	EM122

Bathymetric data processing, fusion, and evaluation were performed to solve the problems of different sources. Independent grid files, such as Gridmb 1(I, J) and Gridmb 2(I, J), were maintained using the Gauss weighted average method for the multibeam data from different cruises. The grid files of Gridmb(I, J) with the same resolution were merged. The GEBCO grid file, which is referred to as Gridgebc0(I, J), was maintained through Gaussian spline interpolation or the Gauss weighted average method. Data accuracy was assessed using the layer overlay comparison method. Finally, data fusion, cutting, and splitting of the bathymetric data were performed. The error (Δd) in the overlapping area data was chosen as the criterion used for correcting the errors in the nonoverlapping area. As

discreet data, $\Delta d(I, J)$ was calculated using $\text{Gridmb}(I, J)$ subtracting $\text{Gridgebc}(I, J)$. $\Delta d(I, J)$ was gridded into the Griderror based on the grid spacing of Gridmb through the trend surface analysis method. The corrected $\text{Gridgebc}_{\text{correct}}(I, J)$ data were obtained using $\text{Gridgebc}(I, J)$ plus $\text{Griderror}(I, J)$. Finally, $\text{Gridgebc}_{\text{correct}}(I, J)$ was cut and merged with $\text{Gridmb}(I, J)$.

The bathymetric and BI data were projected onto the Mercator coordinate system to facilitate the spatial analysis. The “Raster Surface-Slope Tool” and the “Terrain Position Index Tool” of ArcGIS were utilized to extract depth, slope, bathymetric position index (BPI), and BI (Table S1). The depth, slope, BPI, and BI data were used to recognize the geomorphological features around the studied guyots. The BPI is an effective parameter for identifying relatively high and low terrains and is regarded as a good indicator for gullies and channels on aprons [7]. Meanwhile, the BI represents the soft or rough degree of a seabed, which is used to identify the landslide range [3].

The software of Global Mapper (v23.1) was used to estimate the area of various geomorphic features. In addition, cross-sectional profiles of the terrain were extracted at 5 km intervals between gullies and channels, and parameters such as width, relief, and slope on both sides were derived from the profiles. Following the methodology described by Symons et al. [22], Global Mapper was utilized to extract parameters such as the wavelength, wave height, and slope of sediment wave deposits. The results of these analyses are presented in Table S2.

The scarps were outlined on the guyots in the study area, Madeira Island in the Atlantic [17,35] and the Comoros Islands in the Indian Ocean [12,36]. The trajectory curves of the scarps were extracted from various locations to analyze their morphologies and were classified into three types: invagination-arc-, convex-arc-, and complex-arc-shaped scarps (Figure 2). Invagination-arc-shaped scarps are characterized by inward curvature features, such as Lamont AP-02, and convex-arc-shaped scarps are characterized by outward curvature features observed in Arnold AP-01 and Zhinyv AP-07. Complex-arc-shaped scarps extend over longer distances and exhibit a combination of inward and outward curvatures, such as Arnold AP-04 and Lamont AP-01.

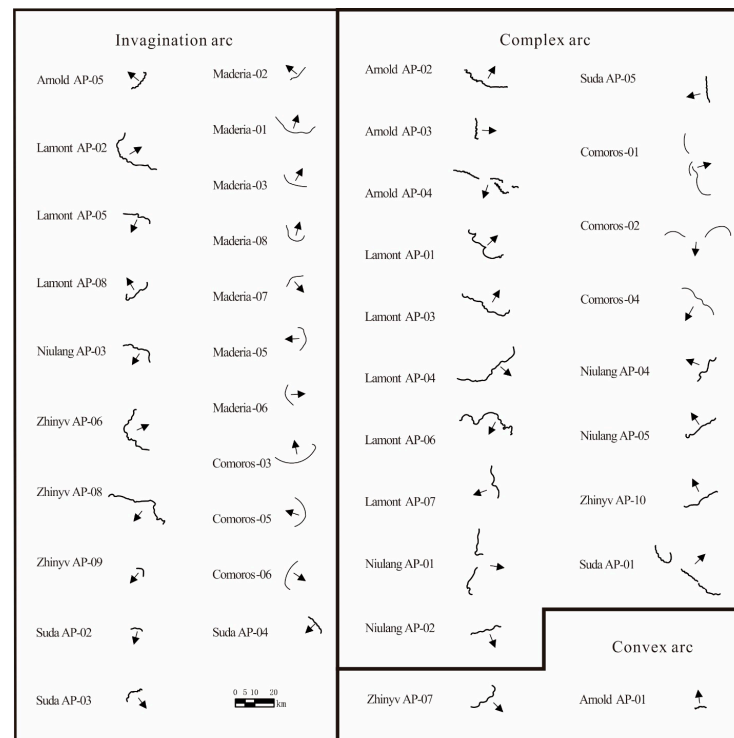


Figure 2. Trajectory curves of the landslide scarps on the studied seamounts, Madeira Island [17] and the Comoros Islands [12].

4. Results

4.1. Suda Guyot

The Suda guyot exhibits a semicircular summit at a depth of ~1300–1500 m and is scattered with small-size volcanic cones, encompassing an area of ~300 km². Five landslide deposits (i.e., Suda AP-01 to Suda AP-05) with varying sizes are identified, corresponding to the scarps observed on the junctions between the summit and slope (Figure 3). Additionally, the presence of morphology characteristics related to landslides, such as gullies, channels, and sediment waves, are identified around the Suda guyot.

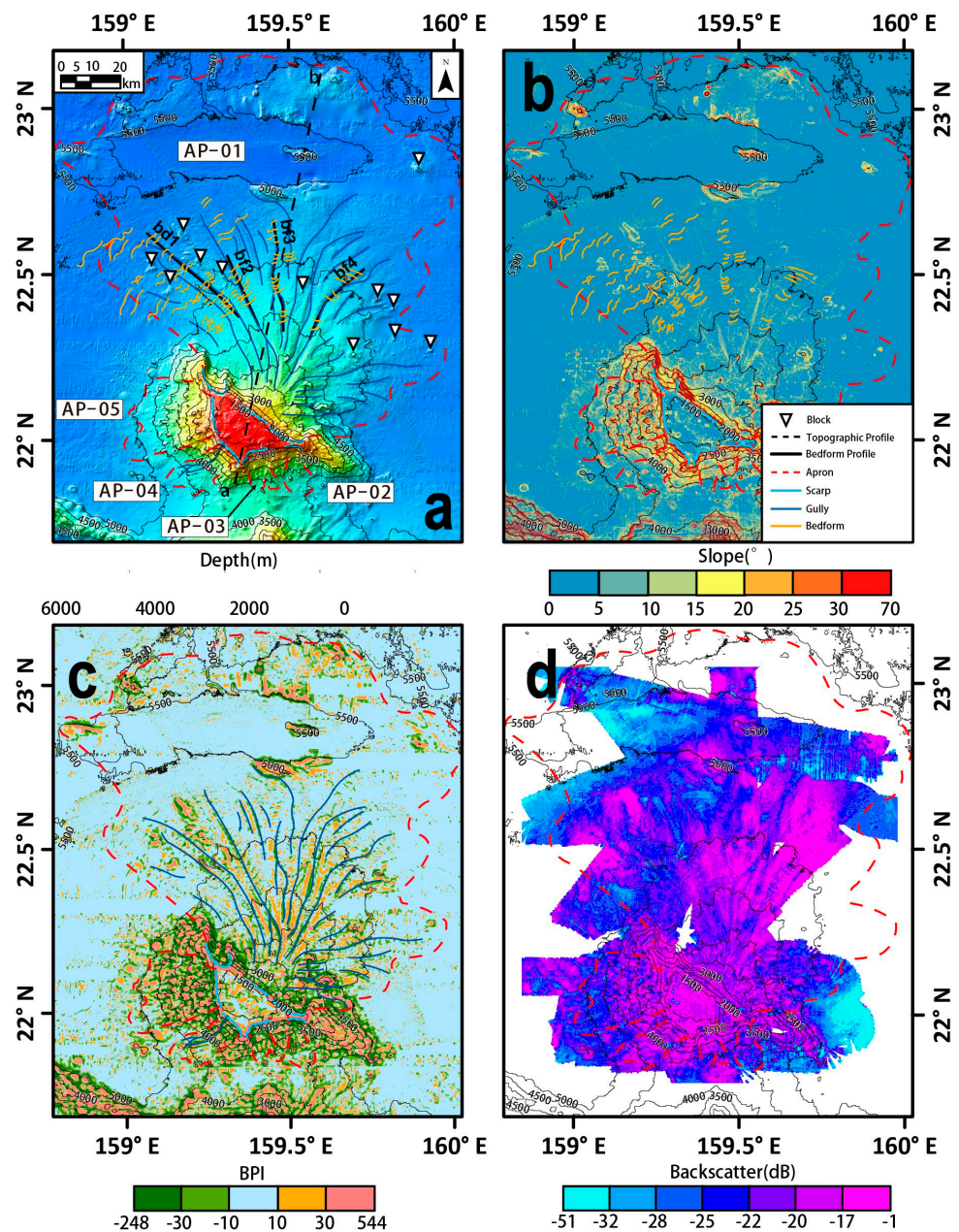


Figure 3. Topography (a), slope (b), BPI (c), and BI (d) of the Suda guyot. Triangles represent blocks, light blue lines represent the scarps of the landslides, dark blue lines represent the gullies, black lines represent the channels, and dotted red lines represent the outline of the depositional lobes of the aprons.

Suda AP-01 (S1) is located in the northeastern area of the guyot; the scarp spans a length of ~42 km, and it features a complex-arc shape. Notably, a depression zone is found

75–100 km north of the scarp. At the heart of the zone lies a knoll, measuring ~10 km in length, ~2.5 km in width, and standing at a height of ~500 m. The slopes on either side of the knoll exhibit an inclination of ~30° (Figure S1). The landslide deposit below the scarp reveals an overall flat terrain, covering an area of ~11,000 km² with an average BI of ~−31 dB. Branching channels and gullies that diverge downward are identified by a low BPI on the lower slope. Within the channels of the deposit, crescent-shaped wave sediment deposits with upslope asymmetry developed (bf1–bf3, Figure S3), which are probably caused by the scouring effects of supercritical fluid [22].

Suda AP-02 (S2) and Suda AP-03 (S3) are situated on the southeastern side of the Suda guyot, and their scarps exhibit invagination-arc shapes with lengths of ~6 and ~13 km, respectively. The lower slope area of the Suda AP-03 exhibits high relief with an average slope of 7.5° compared to that of the Suda AP-02 area with an average slope of 2.5°. The average BI for both areas was relatively similar, with ~−21.5 dB for Suda AP-02 and −19.5 dB for Suda AP-03. Small blocks are visible, and no sediment wave deposits are observed in the two areas.

Suda AP-04 (S4) lies on the southwestern side of the guyot, and its invagination-arc-shaped scarp spans ~11 km in length. The landslide deposit exhibits a gentle slope and an average BI of ~−19 dB. Interlaced gullies and scattered blocks are observed in this area, but no sediment waves are found.

Suda AP-05 (S5) is situated on the western summit, and its complex-arc-shaped scarp spans ~14 km in length. The landslide deposit exhibits a gentle slope and an average BI of ~−21.5 dB. Furthermore, small blocks are found, and no gully or sediment waves are observed.

4.2. Arnold Guyot

The Arnold guyot exhibits a rectangular summit at a depth of ~1350–1500 m and some small volcanic cones adjacent to a 50 km long east–west ridge on its western side. Five landslide areas (i.e., Arnold AP-01 to Arnold AP-05) with varying sizes are identified, corresponding to the scarps (Figure 4).

Arnold AP-01 (A1) is located on the northeastern side of the guyot, and its convex-arc-shaped scarp spans ~7 km in length. Independent blocks with a volume of ~20 km³ lie 80 km north of the scarp (Figure S2). The landslide deposit exhibits an overall flat terrain with an average BI of ~−24 dB. Branching channels and gullies that diverge downward are found on the lower slope and are observed by a low BPI (in the range −10–10). The cross-sectional profiles of the western (bf1) and eastern (bf2) parts of the apron (Figure S4) exhibit upslope asymmetric and symmetric morphology, characterized by sinuous and crescent-shaped sediment wave peaks. These features are supposed to be related to the scouring effects caused by submarine debris [22].

Arnold AP-02 (A2) lies on the northeastern side of the guyot, and its scarp displays a complex-arc shape with a length of ~30 km. The average slope and BI are 3° and −28.5 dB in the deposit, respectively. The cross-sectional profile (bf3) demonstrates the presence of wave sediment, with larger wavelengths ranging from 1507 to 4228 m and smaller wave heights ranging from 5.6 to 15.3 m (Figure S4). Straight wave peaks and symmetric cross-sectional shapes are typical characteristics of large-scale wave sediment deposits [37].

Arnold AP-03 (A3) is located on the eastern side of the guyot, and its complex-arc-shaped scarp spans a length of ~14 km. The landslide deposit exhibits a gentle slope and an average BI of ~−33 dB. No gullies or wave sediment deposits are observed. Notably, considerable large protrusions are densely and similar radially distributed on the deposit, with sizes ranging from 400 to 3000 m. In contrast, similar radial distribution is lacking in the northwest Pacific Ocean, leading us to believe that the prominences in AP-03 are more likely to be blocks rather than volcanic cones.

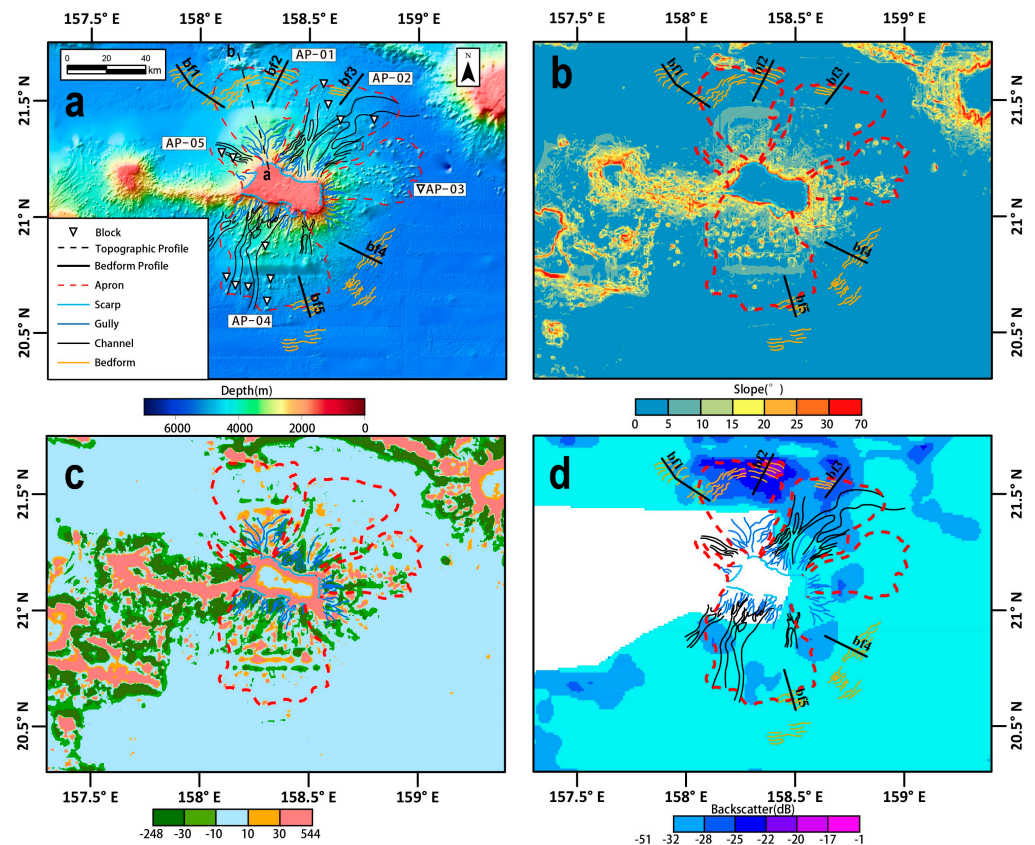


Figure 4. Topography (a), slope (b), BPI (c), and BI (d) of the Arnold guyot. Triangles represent blocks, light blue lines represent the scarps of the landsides, dark blue lines represent the gullies, black lines represent the channels, and dotted red lines represent the outline of the depositional lobes of the aprons.

Arnold AP-04 (A4) lies on the southern side of the guyot, and its complex-arc-shaped scarp spans a length of ~41 km. The lower scarp displays a secondary platform, probably resulting from the continuing small-scale landslide events [38,39]. The landslide deposit exhibits a gentle slope and an average BI of ~−34 dB. Interlaced gullies and scattered blocks are observed, and the large-scale waves sediment deposit display sinuous wave peaks and a symmetric cross-sectional shape (Figure S4).

Arnold AP-05 (A5) lies on the northwestern side of the guyot, and its invagination-arc-shaped scarp spans a length of ~14 km. The landslide deposit exhibits higher relief, with an average slope of 5°. Furthermore, block and wave sediment deposits are not observed.

4.3. Lamont Guyot

The Lamont guyot exhibits a strip-like summit at a depth of ~1300–1800 m. It encompasses an area of ~2000 km² and is adjacent to a 100 km east–west ridge on its western side. Eight landslide areas (i.e., Lamont AP-01 to Lamont AP-08) are identified, corresponding to the scarps (Figure 5).

Lamont AP-01 (L1) is located on the northern side of the guyot, and its complex-arc-shaped scarp spans ~33 km in length. The landslide deposit exhibits an overall flat terrain and an average BI of ~−35 dB. The channels and gullies are parallel and diverge downward and are observed by the low BPI in the range of −100–−20 dB. Small blocks are found, but no wave sediment deposit is observed.

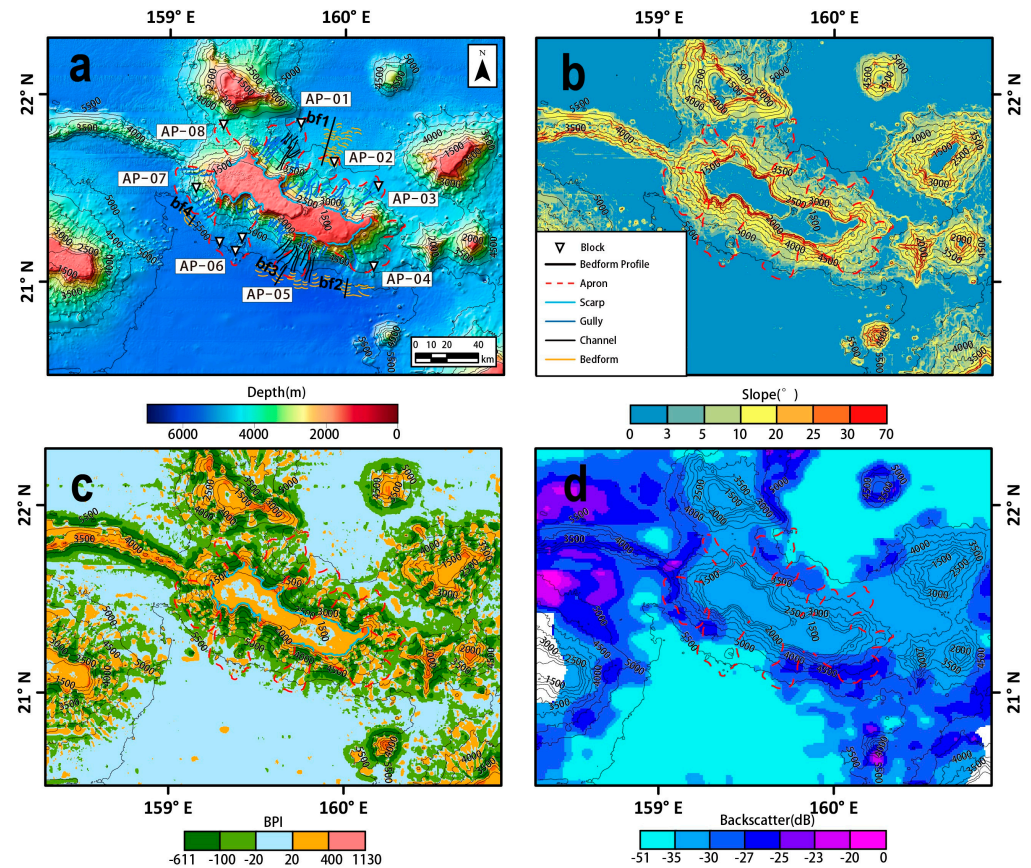


Figure 5. Topography (a), slope (b), BPI (c), and BI (d) of the Lamont guyot. Triangles represent blocks, light blue lines represent the scarps of the landslides, dark blue lines represent the gullies, black lines represent the channels, and dotted red lines represent the outline of the depositional lobes of the aprons.

Lamont AP-02 (L2) lies on the northern side of the guyot, and its invagination-arc-shaped scarp spans ~37 km in length. The landslide deposit exhibits a gentle relief and an average BI of ~−35 dB. Interlaced gullies and scattered blocks are found. Wave sediment deposits are observed with crescentic wave peaks and a symmetric cross-sectional shape (Figure S5).

Lamont AP-03 (L3) is situated on the northeastern side of the guyot, and its complex-arc-shaped scarp spans ~32 km in length. The landslide deposit exhibits an average slope of ~5° and an average BI of ~−35 dB. Nearly parallel, downward-converging gullies are observed.

Lamont AP-04 (L4) lies on the eastern side of the guyot, and its complex-arc-shaped scarp spans ~41 km in length. The landslide deposit exhibits high relief with an average slope of 7° and an average BI of ~−35 dB. Small blocks and two parallel gullies are found. No wave sediment deposit is observed.

Lamont AP-05 (L5) is located on the southern side of the guyot, and its invagination-arc-shaped scarp spans ~17 km in length. The landslide deposit exhibits a gentle slope and an average BI of ~−31 dB. Parallel gullies and channels and wave sediment deposits with reverse crescentic wave peaks and symmetric cross-sections are observed (Figure S5).

Lamont AP-06 (A6) lies on the southwestern side of the guyot. Its complex-arc-shaped scarp spans ~48 km in length and exhibits an invagination arc shape for three segments. The landslide deposit exhibits a gentle slope and an average BI of ~−34.5 dB. Small blocks and converging gullies are found.

Lamont AP-07 (L7) is located on the western side of the guyot, and its complex-arc-shaped scarp spans ~19 km in length with an irregular shape. The landslide deposit exhibits

an overall flat terrain with an average BI of ~ -33.5 dB. Interlaced channels and gullies that diverge downward are found in the lower slope. Small blocks and sediment waves with reverse crescentic wave peak morphologies and symmetric cross-sectional shapes are observed (Figure S5).

Lamont AP-08 (L8) lies on the western side of the guyot, and its invagination-arc-shaped scarp spans ~ 19 km in length and exhibits an internal shape. The landslide deposit exhibits a flat terrain with an average slope of 3° and an average BI of ~ -34.5 dB. No block, gully, or wave sediment deposits are observed.

4.4. Niulang Guyot

The Niulang guyot is adjacent to the Zhinyv guyot, and ten landslide areas are identified around the two guyots (Figure 6). The Niulang Guyot exhibits an irregular summit with a depth ranging from 1600 to 1900 m, encompassing an area of ~ 1000 km². Five landslide areas (i.e., Niulang AP-01 to Niulang AP-05) are identified, corresponding to the scarps.

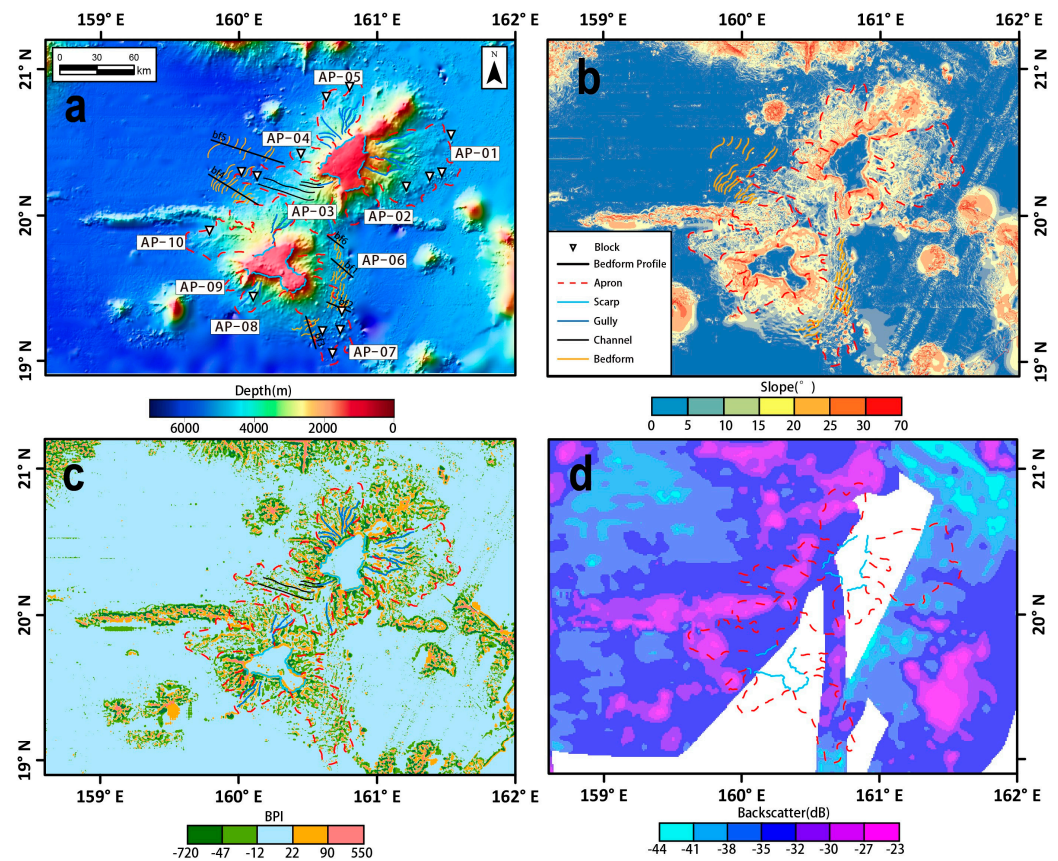


Figure 6. Topography (a), slope (b), BPI (c), and BI (d) of the Niulang and Zhinyv guyots. Triangles represent blocks, light blue lines represent the scarps of the landslides, dark blue lines represent the gullies, black lines represent the channels, and dotted red lines represent the outline of the depositional lobes of the aprons.

Niulang AP-01 (N1) is located on the eastern side of the guyot, and the total length of its complex-arc-shaped scarp with two segments ~ 35 km. The landslide deposit exhibits a gentle slope and an average BI of ~ -36 dB. Interlaced gullies and scattered blocks are observed.

Niulang AP-02 (N2) is located on the southeastern side of the guyot, and its complex-arc-shaped scarp spans ~ 17 km in length. The landslide deposit exhibits a gentle slope

of $\sim 5^\circ$ and an average BI of ~ -24 dB. Large blocks are visible, and no sediment wave is observed.

Niulang AP-03 (N3) lies on the southwestern side of the guyot, and its invagination-arc-shaped scarp spans a length of approximately 20 km. The landslide deposit exhibits a gentle slope and has an average BI of about -34.5 dB. Crescent-shaped sediment wave deposits with symmetric cross-sectional shapes occur (bf5, Figure S6), which have higher relief than sinuous-shaped sediment waves (bf6, Figure S6).

Niulang AP-04 (N4) is located on the western side of the guyot, and its complex-arc-shaped scarp spans a length of ~ 19 km. The landslide deposit exhibits a gentle slope and an average BI of ~ -34.5 dB. Furthermore, no gullies, blocks, or sediment waves are observed in this area.

Niulang AP-05 (N5) lies on the northwestern side of the guyot, and its complex-arc-shaped scarp spans a length of ~ 21 km. The landslide deposit exhibits an overall flat terrain with an average BI of ~ -34.5 dB. Branching channels and gullies that diverge downward occur on the lower slope, but no sediment waves are observed.

4.5. Zhinyv Guyot

The Zhinyv guyot has an irregular summit at a depth of about 1200–1500 m, encompassing an area of approximately 900 km². Five landslide areas (namely from Zhinyv AP-06 to Zhinyv AP-10, respectively) are identified (Figure 6).

ZhiyvAP-06 (Z6) is located on the eastern side of the guyot, and its invagination-arc-shaped scarp spans a length of ~ 34 km. The landslide deposit exhibits an overall flat terrain with an average slope of $\sim 5^\circ$. Symmetrical waves sediment deposits with morphology upslope sinuous morphologies are observed (Figure S6).

Zhinyv AP-07 (Z7) is located on the southeastern side of the guyot, and its convex-arc-shaped scarp spans a length of ~ 20 km. The landslide deposit exhibits a gentle slope and an average BI of ~ -32 dB. Interlaced scattered blocks are observed. Furthermore, no gullies or sediment waves are observed. Symmetrical cross-sections with sinuous wave peaks developed on both sides (bf2–bf3, Figure S6).

Zhinyv AP-08 (Z8) is situated on the southwestern side of the guyot, and its invagination-arc-shaped scarp spans a length of ~ 42 km. The landslide deposit exhibits an overall flat terrain with downslope-directed gullies.

Zhinyv AP-09 (Z9) lies on the western side of the guyot, and its invagination-arc-shaped scarp spans a length of approximately 7 km. The landslide deposit exhibits a slope of 7° and has an average BI of about -30.5 dB. Interlaced gullies and scattered blocks are observed.

Zhinyv AP-10 (Z10) is located on the western side of the guyot, and its complex-arc-shaped scarp spans a length of ~ 20 km. Notably, the landslide deposit is divided into northern and southern parts by the ridge, exhibiting an overall flat terrain, both with an average BI of ~ -34.5 dB. Two main gullies, which are symmetrical to upslope asymmetrical sediment waves with crescentic peaks, occur on the north side (bf4, Figure S6).

5. Discussion

5.1. Landslide Processes and Their Constraints on the Archipelagic Aprons

Landslide processes mainly include slumps, debris avalanches, debris flows, and sediment failures [40]. The formation of archipelagic aprons is believed to result from superimposed processes of contemporaneous or multi-stage landslide events [14]. The morphology of archipelagic aprons probably reveals material types and flowing processes for volcanic materials or sediment emplacement caused by slope failure [14,41]. For relatively younger seamounts (islands), such as the Canary Islands on the eastern Atlantic Ocean off the northwest African margin, a cohesive flow may be composed of fine-grained emplacing materials which result in elongated-shaped debris avalanches, while cohesionless flows with coarse-grained or blocked dominated materials mainly cause fan-shaped deposits [14]. The plotting of the relationships between the morphological parameters of

debris avalanches can provide information relevant to landslide processes in archipelagic aprons [3,14].

Obvious distinctions were presented in the domains and morphologies of the landslide deposits on the ancient guyots. Six debris avalanches had occurred on the Suda, Arnold, Niulang, and Zhinyv guyots, such as Suda AP-04; Arnold AP-05; Niulang AP-02; Zhinyv AP-06, 08, and 10, which belonged to the elongated-shaped deposits (Figure 7). Catastrophic landslides triggered cohesive flows downslope for volcanic materials with a proportion of pyroclastic clasts [41] and sediments. These debris avalanches mainly exhibited relatively flattened topographies and elongated morphologies. Thirteen debris avalanches corresponding to landslides were found to be fan-shaped deposits (Figure 7). Most of these debris avalanches exhibited block-dominated morphologies, except for Lamont AP-07, which was believed to be caused by a cohesionless flow composed of volcanic blocks [41]. Huge volcanic blocks have been found on distal landslide deposits on Suda AP-01 and Arnold AP-01, which probably indicate the occurrences of slumps caused by earlier slope failures. After that, debris avalanches composed of fine-grained materials conducted cohesive flow along the domains confined by slumps. Lamont AP-07 actually presented a rectangular rather than fan-shaped morphology, which corresponded to several second-class landslide scarps. We believe that the landslide deposits on Lamont AP-07 were probably composed of several debris avalanches with cohesive flows of fine coarse materials. Some debris avalanches, including Suda AP-02, 03; Lamont AP-01, 04 and 08; Niulang AP-03; and Zhinyv Ap-09, will not be discussed, because the morphology of these deposits was affected by landslide events which originated from neighboring guyots.

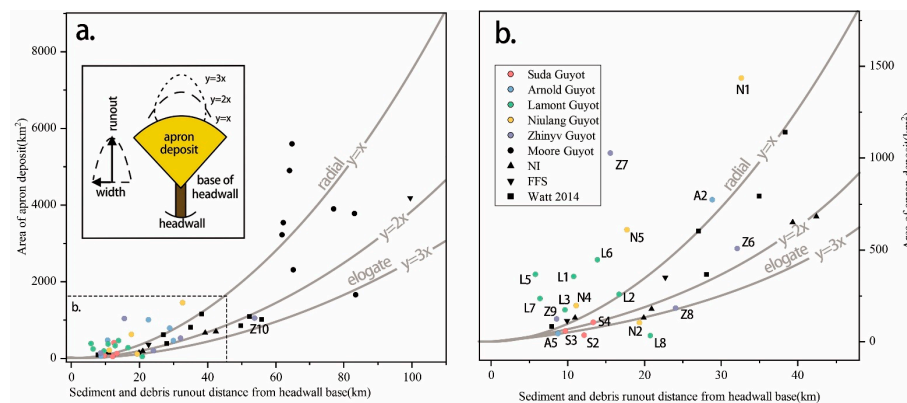


Figure 7. (a) Relationship between area of debris avalanches and extent of landslide (modified from Watt et al. [14]). (b) Enlarged view of the dotted box area in (a). Red represents Suda guyot, blue represents Arnold guyot, green represents Lamont guyot, yellow represents Niulang guyot, and purple represents Zhinyv guyot. Data from previous studies were from Gardner et al. [3], Watt et al. [14], and Muller et al. [26].

The smoother-surfaced regions of the seafloor were believed to result from sediment failures, which occurred on landslide deposits such as Montserrat Lesser Antilles [20]. We did not find this type of landslide deposit on the studied guyots, which was illustrated by the plots of debris avalanche distances and masses and the destruction of seafloor sediments (Figure 8). However, the ubiquitous distribution of channels on the debris avalanches in the studied guyots indicated the dominant debris flows composed of sediment materials in recent times. We envisaged that the superimposition of debris flows and sedimentation dominated in the ancient stage of the seamounts and also buried or changed the previous morphology of the landslide deposits.

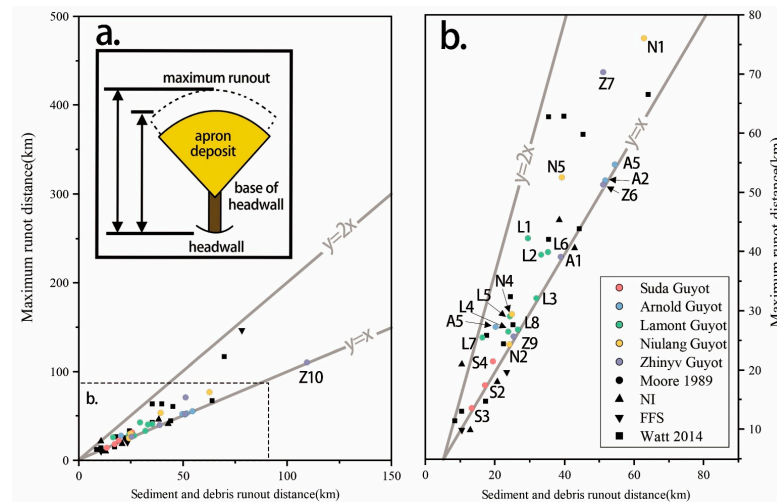


Figure 8. (a) Relationship between debris avalanche distance traveled by debris, sediments, and masses and the destruction of seafloor sediments caused by their emplacement. (b) Enlarged view of the dotted box area in (a). Red represents Suda guyot, blue represents Arnold guyot, green represents Lamont guyot, yellow represents Niulang guyot, and purple represents Zhinyv guyot. Data from previous studies were from Watt et al. [14].

5.2. Scarp Morphologies and Relations with the Domain of the Archipelagic Aprons

Scarps occurring at junctions between summits and slopes mostly exhibit arc-shaped distributions, which are indicative of underlying faults [24] or past landslide events [17,42]. The morphology of scarps can be influenced by a combination of factors, such as rock properties, faults, and surface runoff [24]. Volcanic activities on Madeira Island in the Atlantic Ocean continued from 7 Ma years to the Holocene [35], whereas those on the Comoros Archipelago in the Indian Ocean started in the Pliocene for about 10 Ma years. [36]. Both relatively young seamounts are predominated by invagination-arc-shaped scarps, and debris flows are prone to occur on the landslide deposits. However, more than half of the landslide areas, comprising over 52% of the five ancient guyots in the study area, exhibited complex-arc-shaped scarps. The occurrence of complex-arc-shaped scarps suggests that these seamounts have experienced long and multiple episodes of instability and subsequent landslides over time.

The archipelagic aprons around seamounts are most probably related to scarp morphologies. The plots of the scarp length against the corresponding apron areas in the study area indicate that convex-arc-shaped scarps would belong a wider apron and invagination-arc-shaped scarps would accompany a narrower apron (Figure 9). For example, the area of Arnold AP-01 with a convex-arc-shaped scarp is approximately 10 times larger than that of Zhinyv AP-09 with invagination-arc-shaped scarps, even though the two aprons have similar lengths of scarps and similar heights of falls between the top and base of the seamount (~1350–5400 m). Convex-arc-shaped scarps are not common; it is possible that after a major landslide, later flank failure modified the shape of an original scarp into a convex-arc shape. As a result, the apron below the convex-arc-shaped scarp shows a larger range. We assumed that the invagination-arc-shaped scarps tended to gather and transport fragmented rock masses and sediments over longer distances, which would contribute to the elongated morphologies of the deposits and restrict the development of channels and gullies. This is well confirmed on La Reunion Island [15]. In contrast, landslides with convex-arc-shaped scarps are commonly associated with slump events in the guyots in the study area, which could cause landslides with larger volumes and potential energy levels. This would reduce constraints on the direction of landslide motion, allowing for more extensive movement across the seafloor.

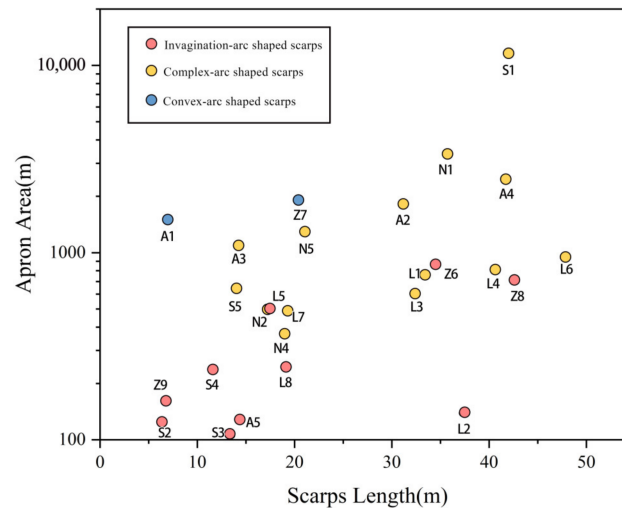


Figure 9. Correlation between the scarps' length and apron area. Red represents invagination-arc-shaped scarps, yellow represents complex-arc-shaped scarps, and blue represents convex-arc-shaped scarps.

5.3. Gully/Channel Morphology and Occurrence

The presence of gullies and channels related to landslides reflects the erosional processes and sediment transport mechanisms associated with gravity flows. Gullies are typically formed directly adjacent to the upper part of aprons and exhibit a V-shaped cross-section, which serve as conduits for the convergence of debris and sediment to the downslope. Gullies are often characterized by steep sidewalls and a narrow channel, indicating the erosional action of gravity flows. Conversely, channels are mostly distributed in the middle and lower slopes of aprons. Channels mostly exhibit a predominantly U-shaped cross-section and are wider and more open compared to gullies. Channels serve as pathways for the transportation of debris, blocks, and sediments downslope [17], which is regarded as a crucial process affecting the redistribution of material from the summit to the apron areas.

The statistical results regarding gullies' and channels' morphological parameters in the study area (Figures S6–S8) indicated that most gullies and channels exhibited slopes $< 10^\circ$, which have a negative correlation with width and a positive correlation with relief. Wide gullies with higher relief have a larger capacity to accommodate sediment transport and deposition, resulting in flat terrain. The divergent gullies and channels in the study area are mostly prone to occurring on fan-shaped aprons with few block structures. The presence of a more developed gully and channel system can be found on Suda AP-01 compared to other areas within the study region. However, in landslide areas such as Lamont AP-02 and Lamont AP-05, where elongated aprons are present, the formation of convergent gully and channel systems is more prominent. In these cases, the formation of rock failures does not involve long-distance movement by gravity flows. The dispersion of block materials makes the formation of gullies less likely.

5.4. Sediment Waves on the Bedforms

The geomorphic characteristics of sediment waves reveal gravity flow processes related to landslides [22]. Small-scale sediment waves are caused by gravity flow scouring and the undulation of basements, whereas large-scale ones are formed by sediment creep at the distal end of an apron.

The ubiquitous occurrences of large-scale sediment wave deposits on the aprons indicated the complex dynamics of sediment transport and deposition on the studied guyots. The Lamont guyot exhibited reverse-crescent symmetric waves, whereas the Arnold guyot displayed sinuous asymmetric waves. The Niulang and Zhinyv guyots exhibited symmetric sinuous waves. The observed wavelengths of the large-scale sediment

wave in the study area extended beyond 4 km, with a wavelength-to-wave height ratio not exceeding 50:1 (Figures S10–S12). Wave profiles and morphologies suggest variations in sediment transport and depositional processes in these areas; the bf3 profile of the Zhinyv guyot, with its deeper water depths and smaller slope, exhibited complex irregular waveforms, which could be attributed to bottom morphology deformation induced by gravitational forces [22], and the morphology of sediment waves in other areas has obvious regularity and may be formed by scouring.

Small-scale sediment waves were mainly observed in the channels of the Suda guyot apron. These sediment waves had smaller wavelengths, which were mostly below 1500 m, and a wavelength-to-wave height ratio of less than 60:1 (Figures S10–S12); the higher BI in this region suggests the presence of coarse sediment particles. Small-scale sediment waves that lay in the Suda guyot exhibited irregular cross-sections and crescent-shaped crests, indicating scouring by gravity currents. These sediment waves were associated with the transport of coarse-grained material and lacked internal layering [43]. The formation of small-scale sediment waves in the area can be attributed to the interaction between gravity flows and irregular substrates. Gravity flow travels downward along stepped channels, impacting the irregular seafloor and inducing hydraulic jumps. Sediment is entrained and transported upward, forming subcritical flow in some areas and returning to supercritical flow in others (Figure S13).

6. Conclusions

Submarine archipelagic aprons surrounding the ancient guyots in the NW Pacific Ocean are over 80 Ma years old and present many complex morphological characteristics, which are the results of mutual influences of landslides and sedimentation.

Six debris avalanche deposits in the studied guyots represent elongated-shape debris avalanches and are believed to be caused by cohesive material flows. Cohesionless landslide material flows result in fan-shaped debris avalanches in the studied guyots. The mutual influences of slump and cohesive flows are probably the factors that caused the fan-shaped debris avalanche without block distribution on Suda AP-01 and Arnold AP-01.

The ubiquitous occurrence of channels on the landslide deposits indicated that the superimposition of debris flows and sedimentation dominated in the recent stages of the studied guyots. Parallel and convergent gullies and channels mostly occurred on the elongated landslide deposits, while divergent and radial gullies and channels were mostly distributed on the fan-shaped aprons.

Sediment waves occurred on the bedforms of the distal archipelagic apron across all studied guyots due to sediment creep. Small-scale sediment waves were only observed in the channels on the aprons of the Suda guyot.

Supplementary Materials: The following supporting information can be downloaded at <https://www.mdpi.com/article/10.3390/jmse12040670/s1>, Figure S1: (a,b) Topographic profile of the Suda guyot; Figure S2: (a,b) Topographic profile of the Arnold guyot; Figure S3: Sediment wave topography profile of Suda guyot; Figure S4: Sediment wave topography profile of Arnold guyot; Figure S5: Sediment wave topography profile of Lamont guyot; Figure S6: Sediment wave topography profile of Niulang and Zhinyv guyots; Figure S7: Relationship between the width and relief of gullies and channels; Figure S8: Relationship between the width and slope of gullies and channels; Figure S9: Relationship between the relief and slope of gullies and channels; Figure S10: Relationship between the width and height of gullies and channels; Figure S11: Relationship between the wavelength and slope of sediment waves at different scales; Figure S12: Relationship between the wave height and slope of sediment waves at different scales; Figure S13: Small-scale sediment wave formation model (modified from Symons et al. [22]); Table S1: Submarine fan topography data; Table S2: Sediment wave topography data.

Author Contributions: Conceptualization, X.W. and H.L.; methodology, X.W., H.L., F.C., H.W. and Y.C.; software, X.W., W.Z., H.W. and Y.D.; validation, X.W., S.L., X.L., Z.L., F.C. and H.L.; resources, H.L.; data curation, X.W., H.L. and Y.C.; writing—original draft preparation, X.W. and H.L.; writing—review and editing, X.W. and H.L.; visualization, X.W., P.Y., W.M. and H.W.; project administration, H.L. and F.C.; funding acquisition, H.L. All authors have read and agreed to the published version of the manuscript.

Funding: The work of this study is supported by the National Key Research and Development Project (2022YFC2806602), the Polymetallic Nodule Exploration Project in the Contract Area of Beijing Pioneer Hi-tech. Development Corporation, and the National Natural Science Foundation of China (U2244222).

Institutional Review Board Statement: Not applicable.

Informed Consent Statement: Not applicable.

Data Availability Statement: The bathymetric data in this study are available at <https://doi.org/10.5281/zenodo.8411156> (accessed on 5 October 2023).

Acknowledgments: The authors thank the scientific and technic staff and crew members of several Chinese Dayang Cruises for collecting the multibeam survey data.

Conflicts of Interest: Authors Huaiming Li and Hongyi Wang were employed by the company Beijing Pioneer High-tech Corporation. The remaining authors declare that the research was conducted in the absence of any commercial or financial relationships that could be construed as a potential conflict of interest.

References

1. Buchs, D.M.; Cukur, D.; Masago, H.; Garbe-Schönberg, D. Sediment Flow Routing during Formation of Forearc Basins: Constraints from Integrated Analysis of Detrital Pyroxenes and Stratigraphy in the Kumano Basin, Japan. *Earth Planet. Sci. Lett.* **2015**, *414*, 164–175. [CrossRef]
2. Seton, M.; Müller, R.D.; Zahirovic, S.; Gaina, C.; Torsvik, T.; Shephard, G.; Talsma, A.; Gurnis, M.; Turner, M.; Maus, S.; et al. Global Continental and Ocean Basin Reconstructions since 200 Ma. *Earth Sci. Rev.* **2012**, *113*, 212–270. [CrossRef]
3. Gardner, J.V.; Calder, B.R.; Armstrong, A.A. Geomorphometric Descriptions of Archipelagic Aprons off the Southern Flanks of French Frigate Shoals and Necker Island Edifices, Northwest Hawaiian Ridge. *GSA Bull.* **2021**, *133*, 2189–2209. [CrossRef]
4. Koppers, A.A.P.; Staudigel, H.; Duncan, R.A. High-Resolution $^{40}\text{Ar}/^{39}\text{Ar}$ Dating of the Oldest Oceanic Basement Basalts in the Western Pacific Basin: PACIFIC BASIN $^{40}\text{AR}/^{39}\text{AR}$ DATING. *Geochem. Geophys. Geosyst.* **2003**, *4*. [CrossRef]
5. Hein, J.R.; Mizell, K.; Koschinsky, A.; Conrad, T.A. Deep-Ocean Mineral Deposits as a Source of Critical Metals for High- and Green-Technology Applications: Comparison with Land-Based Resources. *Ore Geol. Rev.* **2013**, *51*, 1–14. [CrossRef]
6. Hein, J.; Koschinsky, A. Deep-Ocean Ferromanganese Crusts and Nodules. *Treatise Geochem. Second. Ed.* **2014**, *13*, 273–291. [CrossRef]
7. Li, Z.; Li, H.; Hein, J.R.; Dong, Y.; Wang, M.; Ren, X.; Wu, Z.; Li, X.; Chu, F. A Possible Link between Seamount Sector Collapse and Manganese Nodule Occurrence in the Abyssal Plains, NW Pacific Ocean. *Ore Geol. Rev.* **2021**, *138*, 104378. [CrossRef]
8. Agogue, H.; Lamy, D.; Neal, P.R.; Sogin, M.L.; Herndl, G.J. Water Mass-Specificity of Bacterial Communities in the North Atlantic Revealed by Massively Parallel Sequencing: Bacterial Assemblages in North Atlantic Ocean. *Mol. Ecol.* **2011**, *20*, 258–274. [CrossRef] [PubMed]
9. Baines, A.G.; Cheadle, M.J.; Dick, H.J.B.; Scheirer, A.H.; John, B.E.; Kuszniir, N.J.; Matsumoto, T. Mechanism for Generating the Anomalous Uplift of Oceanic Core Complexes: Atlantis Bank, Southwest Indian Ridge. *Geology* **2003**, *31*, 1105–1108. [CrossRef]
10. Vogt, P.R.; Smoot, N.C. The Geisha Guyots: Multibeam Bathymetry and Morphometric Interpretation. *J. Geophys. Res.* **1984**, *89*, 11085–11107. [CrossRef]
11. Staudigel, H.; Koppers, A.; Plank, T.; Hanan, B. Seamounts in the Subduction Factory. *Oceanography* **2010**, *23*, 176–181. [CrossRef]
12. Tzevahirtzian, A.; Zaragosi, S.; Bachèlery, P.; Biscara, L.; Marchès, E. Submarine Morphology of the Comoros Volcanic Archipelago. *Mar. Geol.* **2021**, *432*, 106383. [CrossRef]
13. Locat, J.; Lee, H.J. Submarine Landslides: Advances and Challenges. *Can. Geotech. J.* **2002**, *39*, 193–212. [CrossRef]
14. Watt, S.; Talling, P.; Hunt, J. New Insights into the Emplacement Dynamics of Volcanic Island Landslides. *Oceanography* **2014**, *27*, 46–57. [CrossRef]
15. Babonneau, N.; Delacourt, C.; Cancouët, R.; Sisavath, E.; Bachèlery, P.; Mazuel, A.; Jorry, S.J.; Deschamps, A.; Ammann, J.; Villeneuve, N. Direct Sediment Transfer from Land to Deep-Sea: Insights into Shallow Multibeam Bathymetry at La Réunion Island. *Mar. Geol.* **2013**, *346*, 47–57. [CrossRef]
16. Babonneau, N.; Villeneuve, N.; Mazuel, A.; Bachèlery, P. Erosion and Volcaniclastic Sedimentation at Piton de La Fournaise: From Source to Deep Marine Environment. In *Active Volcanoes of the Southwest Indian Ocean*; Bachèlery, P., Lenat, J.-F., Di Muro, A., Michon, L., Eds.; Active Volcanoes of the World; Springer: Berlin/Heidelberg, Germany, 2016; pp. 71–90, ISBN 978-3-642-31394-3.

17. Quartau, R. Gravitational, Erosional and Depositional Processes on Volcanic Ocean Islands: Insights from the Submarine Morphology of Madeira Archipelago. *Earth Planet. Sci. Lett.* **2018**, *482*, 288–299. [[CrossRef](#)]
18. Bulmer, M.H.; Wilson, J.B. Comparison of Flat-Topped Stellate Seamounts on Earth's Seafloor with Stellate Domes on Venus Using Side-Scan Sonar and Magellan Synthetic Aperture Radar. *Earth Planet. Sci. Lett.* **1999**, *171*, 277–287. [[CrossRef](#)]
19. Cartigny, M.J.B.; Postma, G.; van den Berg, J.H.; Mastbergen, D.R. A Comparative Study of Sediment Waves and Cyclic Steps Based on Geometries, Internal Structures and Numerical Modeling. *Mar. Geol.* **2011**, *280*, 40–56. [[CrossRef](#)]
20. Watt, S.F.L.; Talling, P.J.; Vardy, M.E.; Masson, D.G.; Henstock, T.J.; Hühnerbach, V.; Minshull, T.A.; Urlaub, M.; Lebas, E.; Le Friant, A.; et al. Widespread and Progressive Seafloor-Sediment Failure Following Volcanic Debris Avalanche Emplacement: Landslide Dynamics and Timing Offshore Montserrat, Lesser Antilles. *Mar. Geol.* **2012**, *323–325*, 69–94. [[CrossRef](#)]
21. Laberg, J.S.; Vorren, T.O. The Trñnadjupet Slide, Offshore Norway: Morphology, Evacuation and Triggering Mechanisms. *Mar. Geol.* **2000**, *171*, 95–144. [[CrossRef](#)]
22. Symons, W.O.; Sumner, E.J.; Talling, P.J.; Cartigny, M.J.B.; Clare, M.A. Large-Scale Sediment Waves and Scours on the Modern Seafloor and Their Implications for the Prevalence of Supercritical Flows. *Mar. Geol.* **2016**, *371*, 130–148. [[CrossRef](#)]
23. Voosen, P. A 'Mind Boggling' 19,000 Seamounts Discovered. *Science* **2023**, *380*, 226–227. [[CrossRef](#)] [[PubMed](#)]
24. Santos, R.; Quartau, R.; da Silveira, A.B.; Ramalho, R.; Rodrigues, A. Gravitational, Erosional, Sedimentary and Volcanic Processes on the Submarine Environment of Selvagens Islands (Madeira Archipelago, Portugal). *Mar. Geol.* **2019**, *415*, 105945. [[CrossRef](#)]
25. Usui, Y.; Yamazaki, T.; Saitoh, M. Changing Abundance of Magnetofossil Morphologies in Pelagic Red Clay Around Minamitorishima, Western North Pacific. *Geochem. Geophys. Geosyst.* **2017**, *18*, 4558–4572. [[CrossRef](#)]
26. Müller, R.D.; Seton, M.; Zahirovic, S.; Williams, S.E.; Matthews, K.J.; Wright, N.M.; Shephard, G.E.; Maloney, K.T.; Barnett-Moore, N.; Hosseinpour, M.; et al. Ocean Basin Evolution and Global-Scale Plate Reorganization Events Since Pangea Breakup. *Annu. Rev. Earth Planet. Sci.* **2016**, *44*, 107–138. [[CrossRef](#)]
27. Pilet, S.; Abe, N.; Rochat, L.; Kaczmarek, M.-A.; Hirano, N.; Machida, S.; Buchs, D.M.; Baumgartner, P.O.; Müntener, O. Pre-Subduction Metasomatic Enrichment of the Oceanic Lithosphere Induced by Plate Flexure. *Nat. Geosci.* **2016**, *9*, 898–903. [[CrossRef](#)]
28. Kaneda, K.; Kodaira, S.; Nishizawa, A.; Morishita, T.; Takahashi, N. Structural Evolution of Preexisting Oceanic Crust through Intraplate Igneous Activities in the Marcus-Wake Seamount Chain. *Geochem. Geophys. Geosyst.* **2010**, *11*, 2010GC003231. [[CrossRef](#)]
29. Janney, P.E.; Castillo, P.R. Isotope Geochemistry of the Darwin Rise Seamounts and the Nature of Long-Term Mantle Dynamics beneath the South Central Pacific. *J. Geophys. Res.* **1999**, *104*, 10571–10589. [[CrossRef](#)]
30. Smith, W.H.F.; Staudigel, H.; Watts, A.B.; Pringle, M.S. The Magellan Seamounts: Early Cretaceous Record of the South Pacific Isotopic and Thermal Anomaly. *J. Geophys. Res.* **1989**, *94*, 10501–10523. [[CrossRef](#)]
31. Smoot, N.C. The Marcus-Wake Seamounts and Guyots as Paleofracture Indicators and Their Relation to the Dutton Ridge. *Mar. Geol.* **1989**, *88*, 117–131. [[CrossRef](#)]
32. Dutkiewicz, A.; Müller, R.D.; O'Callaghan, S.; Jónasson, H. Census of Seafloor Sediments in the World's Ocean. *Geology* **2015**, *43*, 795–798. [[CrossRef](#)]
33. Nakanishi, M. Topographic Expression of Five Fracture Zones in the Northwestern Pacific Ocean. In *Geophysical Monograph Series*; Pringle, M.S., Sager, W.W., Sliter, W.V., Stein, S., Eds.; American Geophysical Union: Washington, DC, USA, 1993; Volume 77, pp. 121–136, ISBN 978-0-87590-036-0.
34. Becker, J.J.; Sandwell, D.T.; Smith, W.H.F.; Braud, J.; Binder, B.; Depner, J.; Fabre, D.; Factor, J.; Ingalls, S.; Kim, S.-H.; et al. Global Bathymetry and Elevation Data at 30 Arc Seconds Resolution: SRTM30_PLUS. *Mar. Geod.* **2009**, *32*, 355–371. [[CrossRef](#)]
35. Geldmacher, J.; van den Bogaard, P.; Hoernle, K.; Schmincke, H.-U. The $^{40}\text{Ar}/^{39}\text{Ar}$ Age Dating of the Madeira Archipelago and Hotspot Track (Eastern North Atlantic): The $^{40}\text{Ar}/^{39}\text{Ar}$ age dating. *Geochem. Geophys. Geosyst.* **2000**, *1*. [[CrossRef](#)]
36. Pelleter, A.-A.; Caroff, M.; Cordier, C.; Bachelery, P.; Nehlig, P.; Debeuf, D.; Arnaud, N. Melilite-Bearing Lavas in Mayotte (France): An Insight into the Mantle Source below the Comores. *Lithos* **2014**, *208–209*, 281–297. [[CrossRef](#)]
37. Kostaschuk, R.; Villard, P. Flow and Sediment Trans-Port over Large Subaqueous Dunes: Fraser River, Canada. *Sedimentology* **1996**, *43*, 849–863. [[CrossRef](#)]
38. Bergersen, D.D. Geology and Geomorphology of Wodejebato (Sylvania) Guyot, Marshall Islands. In *Geophysical Monograph Series*; Pringle, M.S., Sager, W.W., Sliter, W.V., Stein, S., Eds.; American Geophysical Union: Washington, DC, USA, 1993; Volume 77, pp. 367–385, ISBN 978-0-87590-036-0.
39. Camoin, G.F.; Arnaud-Vanneau, A.; Bergersen, D.D.; Enos, P.; Ebrén, P. Development and Demise of Mid-Oceanic Carbonate Platforms, Wodejebato Guyot (NW Pacific). In *Reefs and Carbonate Platforms in the Pacific and Indian Oceans*; Camoin, G.F., Davies, P.J., Eds.; Blackwell Publishing Ltd.: Oxford, UK, 2009; pp. 39–67, ISBN 978-1-4443-0487-9.
40. Moore, J.G. Prodigious Submarine Landslides on the Hawaiian Ridge. *Int. J. Rock Mech. Min. Sci. Geomech. Abstr.* **1990**, *27*, 220. [[CrossRef](#)]
41. Masson, D.G.; Watts, A.B.; Gee, M.J.R.; Urgeles, R.; Mitchell, N.C.; Le Bas, T.P.; Canals, M. Slope Failures on the Flanks of the Western Canary Islands. *Earth-Sci. Rev.* **2002**, *57*, 1–35. [[CrossRef](#)]

42. McGuire, W.J. Volcano Instability: A Review of Contemporary Themes. *Geol. Soc. Lond. Spec. Publ.* **1996**, *110*, 1–23. [[CrossRef](#)]
43. Paull, C.K.; Ussler, W., III; Cares, D.W.; Lundsten, E.; Covault, J.A.; Maier, K.L.; Xu, J.; Augenstein, S. Origins of Large Crescent-Shaped Bedforms within the Axial Channel of Monterey Canyon, Offshore California. *Geosphere* **2010**, *6*, 755–774. [[CrossRef](#)]

Disclaimer/Publisher’s Note: The statements, opinions and data contained in all publications are solely those of the individual author(s) and contributor(s) and not of MDPI and/or the editor(s). MDPI and/or the editor(s) disclaim responsibility for any injury to people or property resulting from any ideas, methods, instructions or products referred to in the content.